References

[1]Wittliff, C. E., Wilson, M. R., and Hertzberg, A., "The Tailored-Interface Hypersonic Shock Tunnel," *Journal of the Aerospace Sciences*, Vol. 26, No. 4, 1959, pp. 219–228.

[2]Lordi, J. A., Mates, R. E., and Moselle, J. R., "Computer Program for the Numerical Solution of Nonequilibrium Expansions of Reacting Gas Mixtures," NASA CR-472, May 1979.

[3]Chadwick, K. M., Holden, M. S., Korte, J. J., and Anderson, E. C., "Design and Fabrication of a Mach 8 Contoured Nozzle for the LENS Facility," AIAA Paper 96-0585, Jan. 1996.

[4]Albrechcinski, T. A., Boyer, D. W., Chadwick, K. M., and Lordi, J. A., "Calspan's Upgraded 96" Hypersonic Shock Tunnel: Its Development and Application in the Performance of Research and Testing at Higher Enthalpies," AIAA Paper 95-0236, Jan. 1995.

[5]Hanson, R. K., "Advanced Laser-Based Diagnostics for Shock Tube/Tunnel Flows," *Proceedings of the 21st International Symposium on Shock Waves*, edited by A. F. P. Houwing, Panther Publishing, Fyshwick, ACT, Australia, 1997, pp. 27–32.

[6]Wehe, S. D., Baer, D. S., and Hanson, R. K., "Tunable Diode-Laser Absorption Measurements of Temperature, Velocity, and H_2O in Hypervelocity Flows," AIAA Paper 97-3267, July 1997.

[7]Baer, D. S., Nagali, V., Furlong, E. R., and Hanson, R. K., "Scanned- and Fixed-Wavelength Absorption Diagnostics for Combustion Measurements Using Multiplexed Diode Lasers," *AIAA Journal*, Vol. 34, No. 3, 1996, pp. 489–493.

[8]Alkemade, C. T. J., *Metal Vapours in Flames*, Pergamon, Oxford, 1982, Chap. 3.

[9]Volz, U., and Schmoranzer, H., "Precision Lifetime Measurements on Alkali Atoms and on Helium by Beam-Gas-Laser Spectroscopy," *Physica Scripta*, Vol. T65, 1996, pp. 48–56.

[10]Lide, D. R., *CRC Handbook of Chemistry and Physics No. 78*, CRC Press, Boca Raton, FL, 1997, p. 10.

[11]Radzig, A. A., and Smirnov, B. M., *Reference Data on Atoms Molecules and Ions*, Vol. 31, Springer–Verlag Series in Chemical Physics, Springer–Verlag, New York, 1985, p. 112.

R. P. Lucht
Associate Editor

UV Raman and Fluorescence Flame Spectroscopy Using a Sheridon Grating Spectrograph

Joseph A. Wehrmeyer*
Vanderbilt University, Nashville, Tennessee 37235

Introduction

ULTRAVIOLET (UV) Raman and predissociative fluorescence spectroscopy have become well-established techniques for obtaining major and minor species concentration and temperature measurements in flames.[1] Advantages of UV over visible excitation include increased scattering cross sections and high laser pulse energy. However, experimental complexity is also increased, especially with respect to optical filtering. Interference bandpass filters, centered around a particular Raman wavelength, have been used successfully for two-dimensional visible Raman imaging of a single molecular species,[2,3] but such filters degrade in performance moving from visible to UV wavelengths. Typical UV interference bandpass filter specifications include passband transmittances of 20% for bandwidths of 26 nm, with transmittance dropping to 12% for 12-nm bandwidths.[4] As a result, a spectrometer is used almost exclusively with UV Raman to provide spectral separation while still offering adequate detection efficiency. An additional benefit of the spectrometer is that it offers the capability of simultaneously measuring the Raman signals from several molecular species.

Received 20 November 1998; revision received 8 March 1999; accepted for publication 5 April 1999.

*Research Associate Professor, Department of Mechanical Engineering, Box 1592 Station B. Senior Member AIAA.

By the use of spectrometers, instantaneous multispecies UV Raman measurements, containing one dimensionally resolved (linewise) spatial information, have been demonstrated.[5,6] The linewise UV Raman technique, using the 248-nm KrF excimer laser, has been extensively used to probe diluted,[7] swirled,[8] or lifted[9] hydrogen jet diffusion flames and has even been used in investigations of an oil-fired furnace burner,[10] an optically accessible spark ignition engine,[10] and an optically accessible rocket engine.[11] In general these research efforts use some form of filtering to reduce the intensity of Rayleigh and Mie scattered light entering the spectrometer, and hence, stray light interference with the relatively weak Raman signals is reduced. Such filtering consists of either a liquid butyl acetate filter,[5,10,11] with a 10-mm path length providing about three orders of magnitude attenuation at 248 nm, or one or more interference negative-bandpass (notch) filters,[9,10] each one attenuating the Rayleigh and Mie scattering by approximately two orders of magnitude. Both the liquid and notch filters attenuate the Raman signals lying close in wavelength to the Rayleigh line, i.e., the O_2 and CO_2 vibrational Q branches and the H_2 rotational O and S branches. The liquid filter also absorbs all wavelengths shorter than 248 nm, which includes the Raman anti-Stokes signals.

If the stray light performance of the imaging spectrograph used in a UV Raman system were improved, then less filtering would be required, thereby allowing better detection efficiency at wavelengths close to the Rayleigh wavelength and even allowing anti-Stokes wavelength detection for systems where butyl acetate filters would no longer be required. One way to improve the stray light performance of a spectrograph is to use holographically ruled gratings. Overall stray light of a holographic grating is up to a factor of 10 less than for a mechanically ruled grating and has no preferred direction; it radiates diffusely through 2π sr, rather than being higher near the diffraction orders as for mechanically ruled gratings.[12,13] However, holographically ruled gratings have relatively poor diffraction efficiency, especially in the UV, compared to mechanically ruled gratings. By ion etching a holographically ruled grating's curved grooves into triangular grooves, efficiency is greatly improved, but the etching process roughens the grooves' surface, thereby degrading stray light performance. In general all of the previous UV Raman investigations have used either mechanically ruled or ion-etched holographically ruled gratings, but there exists an attractive grating alternative.

Holographically ruled gratings can receive near-triangular groove shapes without ion etching through the Sheridon recording method.[13,14] Thus high efficiency and low stray light are simultaneously obtained in a Sheridon holographically ruled grating. These gratings are not widespread because the typical visible wavelengths used in their creation, coupled with the index of refraction of the photoresist used to create the grooves, limits the optimum efficiency wavelength, or blaze wavelength, to a maximum of 250 nm. Yet for 248-nm KrF excimer laser spectroscopy this is an ideal blaze wavelength. This Technical Note shows an experimental comparison, using UV Raman and fluorescence spectroscopy, between a mechanically ruled and a Sheridon holographically ruled grating to demonstrate the superior stray light performance of the latter grating type.

Experimental

The multispecies, linewise Raman/fluorescence images shown in Fig. 1 are obtained from a slightly lean, propane–O_2 flame produced over a Hencken burner. The output from a Lambda–Physik COMPex 150T narrowband, tunable KrF excimer laser is focused into the flame using a 2-m focal length lens, producing a beam waist of ~1 mm diameter. The laser is tuned to 248.395 nm to minimize the production of either OH or O_2 fluorescence.[15,16] Several O_2 and OH transitions are within the tuning range of the KrF laser, and 248.395 nm does not fall directly on any of these transitions. However, about 5% of the laser's output ranges from 248 to 249 nm, resulting in broadband O_2 or OH excitation and subsequent fluorescence.

Raman and Rayleigh scattering are collected at right angles to the laser beam using a 50-mm-diam, 250-mm-focal-length ($f/5$) fused silica air-spaced doublet, and a second identical lens set focuses the

collected light onto the entrance slit of an imaging spectrograph. The spectrograph is oriented so that the entrance slit's long dimension is parallel to the laser beam, thus imaging several millimeters down the laser beam path. A gated, intensified charge-coupled device (CCD) camera is used to provide the images. No optical filters are used to facilitate the assessment of relative stray light performance between grating types. Ideally, a comparison between two gratings should be made in the same spectrograph. The present comparison uses two separate spectrographs, however, because neither was equipped with both Sheridon holographic and mechanically ruled gratings on a single turret. Thus, the two parts in Fig. 1 correspond to exactly the same experimental conditions except that two different, but similar, spectrographs are used, with one spectrograph containing a mechanically ruled grating and one containing a Sheridon holographic grating. Both spectrographs have Czerny–Turner configurations and are equipped with toroidal mirrors to provide good off-axis focusing.

Results

Figure 1a shows a linewise image using a 1200-groove/mm mechanically ruled grating, blazed for 250 nm. The grating efficiency (its reflectivity in first order with respect to aluminum's reflectivity) ranges from 60 to 80% going from 240 to 270 nm, based on manufacturer's data (specified for light polarized parallel to the grating grooves). The grating is mounted in a Chromex 250IS imaging spectrograph, which has a 250-mm front focal length and a 330-mm back focal length, resulting in an internal magnification of 1.32. The edge of the postflame zone is imaged so that the bottom of Fig. 1a corresponds to room air surrounding the flame and the top corresponds to a position within the postflame zone. Temperatures vary from 300 K at the bottom of Fig. 1a up to a flame temperature of ~3000 K. Thus, the Rayleigh signal is approximately 10 times stronger in the bottom half of Fig. 1a, for room air, as compared to the top half, for the postflame zone. This order of magnitude increase in the Rayleigh signal causes the apparent widening (bottom half in Fig. 1a) of the region where stray light saturates the CCD. Stray light interference swamps the relatively weak Raman signals at the bottom of Fig. 1a and even interferes with the stronger O_2 fluorescence emission bands occurring in the flame imaged in the upper part of Fig. 1a. For the $(B - X)$ $(v' = 0 \leftarrow v'' = 6)$ and $(2 \leftarrow 7)$ O_2 Schumann–Runge transitions excited by the laser's broadband output, the subsequent fluorescence emission bands that lie in the bandwidth of Fig. 1a are as follows: the $(0 \rightarrow 5)(2 \rightarrow 6)$ pair from 239.2 to 240.8 nm, the $(0 \rightarrow 6)(2 \rightarrow 7)$ pair from 247.7 to 249.4 nm, the $(0 \rightarrow 7)(2 \rightarrow 8)$ pair from 256.7 to 258.5 nm, and the $(0 \rightarrow 8)(2 \rightarrow 9)$ pair from 266.3 to 268.2 nm. Only the $(0 \rightarrow 8)(2 \rightarrow 9)$ emission bands, in the upper right of Fig. 1a, are resolved from the intense Rayleigh scattering, with its artificially wide linewidth caused by the relatively poor stray light performance of the grating coupled with the gain and saturation characteristics of the intensified CCD. The gain of the camera's intensifier must be turned down from its maximum setting to allow even the O_2 $(0 \rightarrow 8)(2 \rightarrow 9)$ emission bands to be detected within the limits of the CCD because they sit on top of a relatively strong background pedestal caused by 248-nm stray light that is present everywhere in the image of Fig. 1a. At this low gain setting, the O_2 Stokes Raman Q branch and the N_2 Stokes Raman Q branch are both below the noise floor of the intensified CCD and cannot be detected in a single pulse.

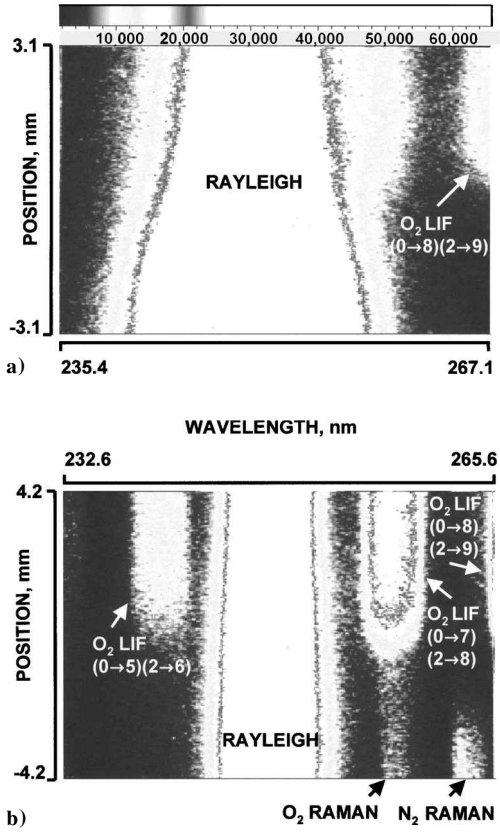

Fig. 1 Single-pulse, linewise UV Raman/fluorescence images at boundary between propane-O_2 flame and air, where O_2 emission lines shown are the result of $(0 \leftarrow 6)$ and $(2 \leftarrow 7)$ excitation by the broadband component of the laser; top, grayscale for signal in A/D counts: a) spectrograph with mechanically ruled grating and 1.32 internal magnification and b) spectrograph with Sheridon holographic grating and 1.00 internal magnification.

Figure 1b shows the same flame, same location, now imaged using a spectrometer equipped with a 1200-groove/mm Sheridon holographically ruled grating, blazed for 250 nm. The grating efficiency ranges from 70 to 80% from 200 to 270 nm, based on the manufacturer's data (specificied for light polarized 45 deg to the grating grooves). The grating is mounted in an Acton 300IS imaging spectrograph, which has 300-mm front and back focal lengths, which produces an internal magnification of one. The reduced internal magnification of the Acton spectrograph compared to the Chromex allows a longer portion of the laser to be imaged: an increase from 6.2 to 8.4 mm. The Rayleigh scattering stray light is significantly suppressed relative to the mechanically ruled grating, which allows the gain of the camera to be increased up to its maximum setting. As a result, both the room air O_2 and N_2 Stokes vibrational Raman bands are apparent in Fig. 1b, as compared to their absence in Fig. 1a. This is because at their physical locations on the CCD there does not coexist appreciable amounts of 248-nm stray light, as was the case in Fig. 1a where 248-nm stray light interference is spread not just in the saturated regions of the CCD (appearing white in Fig. 1a) but also throughout Fig. 1a in intensities at or higher than the Raman signal intensities. For Fig. 1b, the O_2 and N_2 Raman Stokes Q branches are clearly seen, with the N_2 Stokes Q branch disappearing in the N_2-deficient propane–O_2 flame. The O_2 $(0 \rightarrow 5)(2 \rightarrow 6)$ and $(0 \rightarrow 7)(2 \rightarrow 8)$ fluorescence emission bands [again caused by $(0 \leftarrow 6)(2 \leftarrow 7)$ excitation from the broadband laser output] are also spectrally resolved from the 248-nm Rayleigh scattering. These bands are relatively strong compared to the O_2 Raman Stokes Q branch because the 3000 K temperature of this propane–O_2 flame provides high population fractions for both the $v'' = 6$ and 7 vibration levels. This increases the O_2 fluorescence, even tuning away from an O_2 excitation transition, compared to other UV works that investigated lower temperature air-fed flames where the O_2 Raman Stokes Q branch is dominant over the O_2 $(0 \rightarrow 7)(2 \rightarrow 8)$ fluorescence emission band in flame zones.[5–11]

Conclusion

A comparison has been made of the near-diffraction order stray light performance between a mechanically ruled grating and a Sheridon holographically ruled and blazed grating when they are applied to UV laser combustion diagnostics. The present comparison is only qualitative because two spectrographs were used due to equipment limitations. Because of the inherent groove smoothness in the holographic Sheridon grating, it is superior in stray light performance to the classically ruled grating. The limitation of the

Sheridon grating to a maximum blaze wavelength of 250 nm, although precluding its use in visible Raman systems, does not hinder its application to UV Raman or fluorescence spectroscopy because maximum grating efficiency is desirable around 250 nm. Using a Sheridon grating in a spectrograph used for UV laser combustion diagnostics reduces or eliminates the need for Rayleigh/Mie scattering filtering and thus provides more sensitivity in detecting Raman or fluorescence signals lying close in wavelength to the laser line.

Acknowledgment

This work was supported by the National Research Council through a Senior Research Associateship for the author at the NASA Marshall Space Flight Center, Huntsville, Alabama.

References

[1]Rothe, E. W., and Andresen, P., "Application of Tunable Excimer Lasers to Combustion Diagnostics: A Review," *Applied Optics*, Vol. 36, No. 18, 1997, pp. 3971–4033.

[2]Frank, J. H., Lyons, K. M., Marran, D. F., Long, M. B., Stårner, S. H., and Bilger, R. W., "Mixture Fraction Imaging in Turbulent Nonpremixed Hydrocarbon Flames," *Twenty-Fifth Symposium (International) on Combustion*, Combustion Inst., Pittsburgh, PA, 1995, pp. 1159–1164.

[3]Schefer, R. W., Namazian, M., and Kelley, J., "CH, OH, and CH_4 Concentration Measurements in a Lifted Turbulent-Jet Flame," *Twenty-Third Symposium (International) on Combustion*, Combustion Inst., Pittsburgh, PA, 1990, pp. 669–676.

[4]"Optical Filter Catalog," 2nd ed., Corion Corp., Franklin, MA, 1998.

[5]Nandula, S. P., Brown, T. M., Pitz, R. W., and DeBarber, P. A., "Single-Pulse, Simultaneous Multipoint Multispecies Raman Measurements in Turbulent Nonpremixed Jet Flames," *Optics Letters*, Vol. 19, No. 6, 1994, pp. 414–416.

[6]Reckers, W., Hüwel, L., Grünefeld, G., and Andresen, P., "Spatially Resolved Multispecies and Temperature Analysis in Hydrogen Flames," *Applied Optics*, Vol. 32, No. 6, 1993, pp. 907–918.

[7]Chen, Y.-C., and Mansour, M. S., "Measurements of the Detailed Flame Structure in Turbulent H_2–Air Jet Diffusion Flames with Line-Raman/Rayleigh/LIPF-OH Technique," *Twenty-Sixth Symposium (International) on Combustion*, Combustion Inst., Pittsburgh, PA, 1996, pp. 97–103.

[8]Tacke, M. M., Cheng, T. C., Hassel, E. P., and Janicka, J., "Study of Swirling Recirculating Hydrogen Diffusion Flame Using UV Raman Spectroscopy," *Twenty-Sixth Symposium (International) on Combustion*, Combustion Inst., Pittsburgh, PA, 1996, pp. 169–175.

[9]Brockhinke, A., Andresen, P., and Kohse-Höinghaus, K., "Contribution to the Analysis of Temporal and Spatial Structures Near the Lift-Off Region of a Turbulent Hydrogen Diffusion Flame," *Twenty-Sixth Symposium (International) on Combustion*, Combustion Inst., Pittsburgh, PA, 1996, pp. 153–159.

[10]Grünefeld, G., Beushausen, V., Andresen, P., and Hentschel, W., "Spatially Resolved Raman Scattering for Multi-Species and Temperature Analysis in Technically Applied Combustion Systems: Spray Flame and Four-Cylinder In-Line Engine," *Applied Physics B*, Vol. 58, No. 4, 1994, pp. 333–342.

[11]Wehrmeyer, J. A., Cramer, J. M., Eskridge, R. H., and Dobson, C. C., "Ultraviolet Raman Diagnostics for Rocket Engine Injector Development," AIAA Paper 97-2843, July 1997.

[12]Lerner, J. M., and Thevenon, A., *The Optics of Spectroscopy—A Tutorial*, Instruments SA, Inc., Metuchen, NJ, 1986, p. 6.

[13]Loewen, E. G., "Diffraction Gratings, Ruled and Holographic," *Applied Optics and Optical Engineering*, edited by R. R. Shannon and J. C. Wyant, Vol. 9, Academic, New York, 1983, pp. 33–71.

[14]Palmer, C. P., *Diffraction Grating Handbook*, 2nd ed., Milton Roy Co., Rochester, NY, 1994, pp. 15–19.

[15]Wehrmeyer, J. A., Cheng, T.-S., and Pitz, R. W., "Raman Scattering Measurements in Flames Using a Tunable Excimer Laser," *Applied Optics*, Vol. 31, No. 10, 1992, pp. 1495–1504.

[16]Andresen, P., Bath, A., Gröger, W., Lülf, H. W., Meijer, G., and ter Meulen, J. J., "Laser-Induced Fluorescence with Tunable Excimer Lasers as a Possible Method for Instantaneous Temperature Field Measurements at High Pressures: Checks with an Atmospheric Flame," *Applied Optics*, Vol. 27, No. 2, 1988, pp. 365–378.

R. P. Lucht
Associate Editor

Shape Control of Laminated Plates with Piezoelectric Actuators Including Stress-Stiffening Effects

Sérgio Frascino Müller de Almeida*
Instituto Tecnológico de Aeronáutica, 12228-900 São José dos Campos, Brazil

I. Introduction

PIEZOELECTRIC elements can be used as sensors or actuators in applications such as shape control, active damping, and acoustic noise suppression of a wide class of structures. The effective use of these systems requires accurate electromechanical models to simulate the interaction between the structure and the piezoelectric elements. The literature addresses the modeling of piezoelectric elements either bonded or embedded to several different types of structures. The piezoelectric actuation of beams was treated in depth by Crawley and Anderson[1] and Crawley and de Luis.[2] Several other formulations were also developed for the modeling of plates[3,4] and general shells.[5] Most of the electromechanical models proposed in the literature are based on linear analyses.

The piezoelectric elements are usually mounted to the top and bottom surfaces of a structural element and may induce in-plane extension, bending, and localized shear deformations in structural elements.[6] If both elements are actuators and shear deformation is neglected, the in-phase actuation produces in-plane deformations, whereas out-of-phase actuation produces bending. If one of the piezoelectric elements is used as an actuator while the second one is used as a sensor, or if a single piezoelectric actuator is mounted on a surface, the actuation always results in combined in-plane and bending stresses.

The in-plane stresses may have a significant influence on the mechanical behavior of plates. Initial and/or residual stresses affect the flexural stiffness and in turn the dynamic and stability characteristics of laminated plates.[7] The initial and/or residual stresses in a plate may result from a combination of boundary constraints with external applied loads and environmental effects. Almeida and Hansen[8] showed that, with proper design, thermal residual stresses caused by the curing process can be tailored to enhance the mechanical behavior of composite plates. Rammerstorfer[9] determined optimum fields of residual stresses that maximize the first natural frequency and buckling load of plates.

Piezoelectric elements provide great flexibility in inducing in-plane stress fields because the distribution and magnitude of the in-plane stresses can be easily controlled by varying the voltages applied to each actuator. The objective of this work is to investigate the effectiveness of using piezoelectric elements to control the flexural stiffness of composite plates by inducing in-plane stresses. A finite element approach is used to model laminated plates with piezoelectric actuators and/or sensors placed at arbitrary portions of the plate. The analysis assumes ideal linear theory for the piezoelectric actuation and includes stress-stiffness effects. In the case of plates without membrane-bending coupling, the in-plane problem and the bending problem may be independently solved from two subsequent linear analyses. The numeric results on the shape control of laminated plates with piezoelectric actuators demonstrate that even if the plate is unconstrained the piezoelectrically induced in-plane stresses may significantly affect the mechanical behavior of the plate.

II. Problem Formulation

Consider a laminated plate with piezoelectric elements symmetrically bonded to the top and bottom surfaces at arbitrary positions.

Received 25 May 1998; revision received 15 March 1999; accepted for publication 16 March 1999.

*Professor, Department of Mechanical Engineering.